Nanoscale curvature of the plasma membrane regulates mechanoadaptation through nuclear deformation and rupture

Emmet A. Francis[1,2,*], Einollah Sarikhani[3,*], Vrund Patel[3], Dhivya Pushpa Meganathan[3], Zeinab Jahed[3,**], and Padmini Rangamani[1,2,**]

[1]Department of Pharmacology, University of California San Diego, La Jolla, CA, USA
[2]Department of Mechanical and Aerospace Engineering, University of California San Diego, La Jolla, CA, USA
[3]Department of Nanoengineering, University of California San Diego, La Jolla, CA, USA
[*]these two authors contributed equally to this work
[**]all correspondence may be addressed to zjahed@ucsd.edu and prangamani@health.ucsd.edu

Abstract

Nuclear translocation of the transcription regulatory proteins YAP and TAZ is a critical readout of cellular mechanotransduction. Recent experiments have demonstrated that cells on substrates with well-defined nanotopographies exhibit an altered mechanical and signaling response when compared to those on flat substrates, demonstrating mechanoadaptation to geometric constraints. Specifically, such cells show lower rates of focal adhesion formation, resulting in lower amounts of YAP/TAZ nuclear translocation. In this study, we investigate how the crosstalk between substrate nanotopography and mechanotransduction affects cytoskeletal activity and the nuclear transport of YAP/TAZ. We develop a biophysical model that incorporates plasma membrane (PM) curvature-dependent inhibition of integrin-mediated signaling, PM curvature-sensitive actin assembly, and stretch-induced opening of nuclear pore complexes (NPCs) upon indentation of the nuclear envelope (NE) by nanopillars. Our model predicts lower levels of cytoskeletal activation on nanopillar substrates, consistent with experiments. We demonstrate that this effect can be partially compensated for by increasing the indentation of the NE, leading to local cytoskeletal accumulation and enhanced YAP/TAZ transport through stretched NPCs. Nuclear deformation and cytoskeletal arrangement in our model agree well with experimental fluorescence images and electron micrographs of cells on nanopillar substrates. We then use our model to predict the effects of NE rupture on YAP/TAZ nuclear abundance, showing that if nuclear entry is favored over export through these rupture-induced pores, YAP/TAZ accumulates in the nucleus. We confirm this prediction experimentally, showing that nuclear YAP/TAZ increases in cells with ruptured NEs.

Introduction

Mechanotransduction, the set of processes by which cells respond to mechanical cues by altering their signaling response, is critical for integration of chemical and physical stimuli in different physiological environments. Given the wide range of stiffnesses exhibited by tissues throughout the human body [1] and changes in mechanical properties of extracellular matrix (ECM) associated with diseases and aging [2–4], mechanotransduction occupies a pivotal role in cell physiology. However, the manner in which a cell simultaneously responds and adapts to combined mechanical cues such as stiffness, membrane curvature, and other micro- and nano-topographical features remains unclear. Collectively, such cell responses are referred to as mechanoadaptation and are critical for cell migration through diverse extracellular geometries [5, 6].

Engineered substrates with nano-scale features such as nanobars and nanopillars have proven to be a valuable experimental tool to probe cellular responses to nanotopography. Such substrates induce positive (inward) curvature of the plasma membrane (PM), leading to changes in local processes such as endocytosis [7, 8], integrin recruitment [6], and PM-endoplasmic reticulum contact sites [9], as well as whole-cell properties such as cell stiffness [8]. Recent studies indicate that the assembly and remodeling of cytoskeleton-associated molecules is a function of underlying substrate curvature. For instance, cells that spread over nanobars or nanopillars formed adhesion complexes distinct from conventional focal adhesions [6, 10, 11]. These differences in cell-ECM interactions and cytoskeletal assembly contribute to changes in nuclear localization of transcriptional regulatory proteins such as yes-associated protein (YAP) and the closely related protein, PDZ-binding motif (TAZ, also known as WWTR1). It was found that the

extent of YAP nuclear translocation depended not only on substrate stiffness but also on substrate nanotopography [8]. Specifically, recent studies showed that cells grown on stiff substrates with nanopillars showed similar cytoskeletal activity to those grown on flat, soft substrates. An increase in endocytosis of integrins occurring at the inwardly curved regions of the PM resulted in reduced cytoskeletal stiffness and therefore lower YAP nuclear abundance [8]. Separately, nanoscale topographical features have also been shown to enhance nuclear transport. For example, we recently showed that certain cells on nanopillar substrates exhibit nuclear envelope (NE) rupture, leading to rapid transport of molecules across the NE [12].

These recent observations raise new questions regarding YAP/TAZ signaling, one of the best-characterized mechanotransduction pathways leading to changes in gene expression [13]. YAP and TAZ (collectively referred to as YAP/TAZ throughout) are regulated by the Hippo pathway; in particular, LATS1 and LATS2 phosphorylate YAP/TAZ at select serine residues, leading to their sequestration in the cytosol [14]. However, mechanical cues can regulate YAP/TAZ phosphorylation state independently from the Hippo pathway, inducing changes in YAP/TAZ nuclear abundance [15]. Briefly, engagement of integrins in the PM with the extracellular matrix (ECM) triggers tyrosine phosphorylation of focal adhesion kinase (FAK) in an ECM-stiffness-dependent manner [16, 17]. This, in turn, leads to activation of the small GTPase, Ras homolog family member A (RhoA), and Rho-associated protein kinase (ROCK), triggering actin polymerization and myosin activation and allowing for efficient cell motility following assembly of focal adhesion complexes. Formation of focal adhesions is accompanied by dephosphorylation of cytosolic YAP/TAZ, allowing their transmigration into the nucleus through nuclear pore complexes (NPCs). YAP/TAZ then influence gene expression by binding to transcriptional enhanced associate domains (TEADs) [18].

Computational models have previously been used to predict the effects of substrate stiffness, substrate dimensionality, and ligand micropatterns on cytoskeletal activation and YAP/TAZ nuclear translocation in well-mixed and spatial frameworks [19–22]. While these models shed light on the complex interplay between cell geometry and substrate stiffness in cell mechanotransduction, the role of substrate topography and its impact on YAP/TAZ nuclear translocation remains unexplored.

Here, we use a combination of modeling and experiments to investigate how cells integrate nanotopographical cues to generate mechanotransduction responses. Recent development of software to simulate reaction-transport networks in realistic cell geometries [23, 24] enables us to conduct these more detailed simulations of the effects of nanoscale substrate features on mechanotransduction signaling. We first generate model geometries corresponding to cells on different nanopillar substrates and run a series of simulations to calibrate our model to previous measurements of nuclear YAP as a function of nanopillar size and spacing [8]. We then extend this model to describe nuclear transport of YAP/TAZ following nuclear deformation on nanopillars. We relate this to direct measurements of nuclear indentation in U2OS cells and use our model to predict the effect of NE rupture on YAP/TAZ signaling. Finally, we validate our model predictions against experimental measurements, establishing that nuclear rupture can enhance YAP/TAZ nuclear accumulation on nanopillar substrates.

Results

Model summary

Building on previous models in the literature [19, 20], we model YAP/TAZ nuclear translocation as a function of nanotopography. Here, we present a brief summary of the main events included in our baseline model. We introduce additional curvature- and deformation-dependent reactions at the PM and NE as they are simulated. Initially, tyrosine residues of FAK are phosphorylated downstream from integrin binding, in a substrate-stiffness-dependent manner. FAK then activates RhoA and ROCK, leading to actin polymerization and changes in myosin activity (Figure 1A). The formation of stress fibers, indicated by the product of F-actin and activated myosin motors, is assumed to increase the effective rate of YAP/TAZ dephosphorylation in the cytosol. Since we focus on a single cell, we neglect changes to LATS-mediated phosphorylation of YAP/TAZ due to formation of cell-cell contacts or other activation of Hippo signaling. Dephosphorylated YAP/TAZ can transmigrate into the nucleus through NPCs at a rate depending on the extent of cytoskeletal assembly [25]. In particular, it is assumed that lamin A is increasingly dephosphorylated as a function of cytosolic stiffness (a function of F-actin), causing it to be retained at the NE [26] and cooperate with linker of nucleoskeleton and cytoskeleton (LINC) complexes to transmit force to NPCs [27]. Equations governing the reaction and diffusion of each species are given in Supporting Information, Section S2. We simulated these reaction-diffusion equations using our recently developed software package, Spatial Modeling Algorithms for Reaction and Transport (SMART) [23, 24]. Details on our model implementation in SMART, as well as mesh generation using the mesh generator Gmsh [28], are provided in Methods and Supporting Information.

Regulation of FAK phosphorylation and actin polymerization by plasma membrane curvature

We first considered the population-averaged effects of nanopillar size and spacing on YAP/TAZ signaling. Previous experiments have shown that U2OS cells grown on nanopillar substrates behave similarly to those grown on soft substrates, with reduced contact area and lower YAP nuclear to cytosolic ratio (N/C) when compared to cells on flat, stiff substrates [8]. This was attributed to endocytosis of integrins at regions of inward PM curvature on nanopillars.

Accordingly, we adapted our computational model to predict the effects of integrin endocytosis due to membrane curvature (Figure 1A). As in previous work, we assume that the rate of FAK tyrosine phosphorylation depends on both the substrate stiffness [19, 20] and the density of integrin-ligand complexes [19, 21]. In regions of high membrane-curvature, endocytosis lowers the integrin density. Therefore, we introduced an empirical relationship that scales the total rate of FAK phosphorylation at the cell surface, $k_{FAK,tot}$, as a function of the mean curvature of the PM, H_{PM}:

$$k_{FAK,tot} = \begin{cases} k_{FAK}(E_{mod}) \exp\left(-\frac{H_{PM}}{H_0}\right) & H_{PM} \geq 0 \\ k_{FAK}(E_{mod}) & H_{PM} < 0 \end{cases}, \tag{1}$$

where k_{FAK} (E_{mod}) is the FAK phosphorylation rate on a flat substrate of Young's modulus E_{mod} and H_0 is a constant controlling the degree of curvature sensitivity. Note that FAK phosphorylation is reduced for positive (inward) curvatures, but is unaffected in regions of negative curvature under our current set of assumptions. Similar exponential dependencies of reaction rates on membrane curvature have been used in previous models to capture complex interactions [10, 29].

Separate studies have also shown that F-actin assembles at highly curved regions of PM [6, 10, 11]. This has been attributed to formin-binding protein 17 (FBP17)-dependent activation of Neuronal Wiskott–Aldrich syndrome protein (N-WASP), leading to actin polymerization around nano-curved structures [10, 11]. We introduce associated curvature-dependent actin polymerization at the PM in contact with the substrate ($\Gamma_{substrate}$):

$$k_{poly,N\text{-}WASP} = k_{N\text{-}WASP} \exp\left(\frac{H}{H_{N\text{-}WASP}}\right) \quad \text{on } \Gamma_{substrate}, \tag{2}$$

where $k_{N\text{-}WASP}$ is the rate of actin polymerization on flat PM and $H_{N\text{-}WASP}$ is the characteristic curvature governing the exponential relationship. Based on experimental measurements showing that N-WASP activation preferentially occurs on nanobars less than 500 nm in width, we fix $H_{N\text{-}WASP}$ at 2 μm^{-1} (the mean curvature of the curved sides of 500 nm nanobars). We treat $k_{N\text{-}WASP}$ as a free parameter.

Simulations showed that FAK phosphorylation was lower on nanopillar substrates compared to flat substrates with the same stiffness (Figure 1C). Because the total contact area of the PM on nanopillar substrates is much greater than the projected area, the effect on FAK phosphorylation was relatively weak. However, the effect of curvature sensitivity was amplified for downstream RhoA activation (Figure 1D). Consequently, cytoskeletal activation was also appreciably lower, as indicated by the relative density of stress fibers and the overall cytosolic stiffness, which are both defined as functions of activated myosin and/or F-actin (Figure 1E-F).

Looking more closely at the local actin assembly, we observed that simulations of cells on nanopillars exhibited enhanced local actin assembly as expected (Equation (2), Figure 2A-C, Movies 1 to 6). However, the average increase in stress fibers and cytosolic stiffness increase the rate of YAP/TAZ transport into the nucleus via dephosphorylation of cytosolic YAP/TAZ and dephosphorylation of lamin A, respectively. We observed increased nuclear YAP/TAZ in correlation with robust cytoskeletal activation (Figure 2A-D). The extent of agreement of these predictions with experimental data from Li et al. depended on our assumed values for H_0 and k_{WASP}, which remained free parameters in the modified model. Over the values tested, we found that H0 = 5 μm^{-1} and k_{WASP} = 0.01 μm/s yielded the best match with experiments while still showing local actin accumulation on nanopillars (Figure 2E, Figure S1). This agrees well with the finding that clathrin-mediated endocytosis preferentially occurs on nanopillars less than 200 nm in radius [7], which requires a mean PM curvature of at least 2.5 μm^{-1}. Overall, this formulation of the model predicts that, beyond some curvature threshold, the typical response of a cell to stiff ECM surfaces will be inhibited. This finding suggests that curvature sensitivity can serve as a general mechanism for mechanoadaptation in response to surface topography.

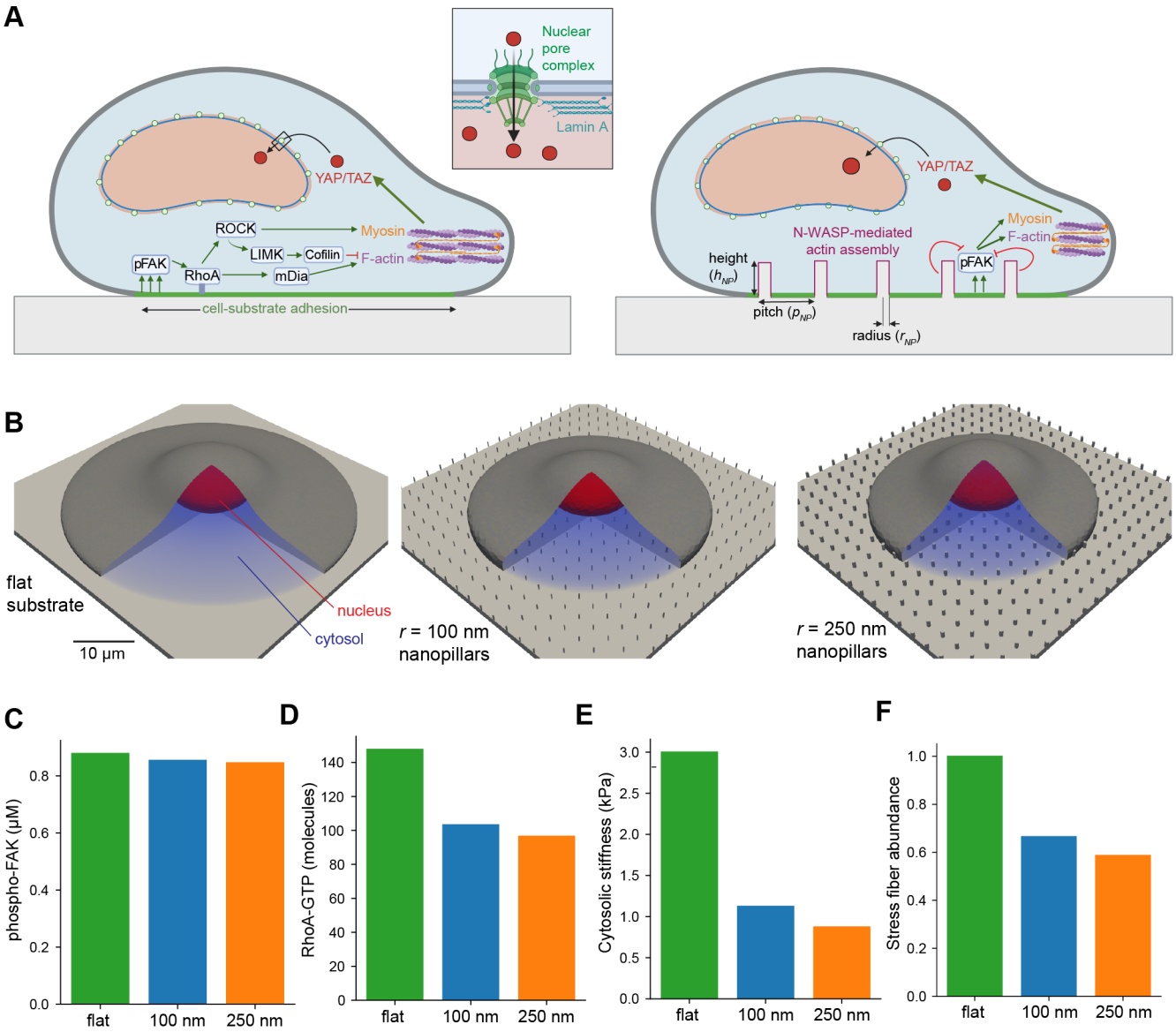

Figure 1: Substrate nanotopography alters activation of enzymes at the plasma membrane and downstream cytoskeletal activation. A) Schematic summarizing the main biochemical events leading to changes in nuclear YAP/TAZ in our model, in the case of a flat substrate (left) and a nanopillar substrate (right). The arrangement of nanopillars is dictated by their height, pitch, and radius, which then affect signaling at the PM in a curvature-dependent manner, by enhancing N-WASP-mediated actin assembly and inhibiting FAK phosphorylation. Inset depicts the arrangement of NPCs and lamin A at the NE. B) Cell geometries on a flat substrate (left) and substrates with nanopillars of radius 100 nm (center) and 250 nm (right). Both nanopillar substrates share the same height (1 μm) and spacing (2.5 μm) of nanopillars. C-F) Phosphorylated FAK concentration, RhoA-GTP molecules at the PM, cytosolic stiffness, and relative stress fiber abundance in the cytosol for all 3 geometries in panel B. All quantities were spatially averaged over the entire relevant compartment and assessed after reaching steady-state (t = 10,000 s) for $H_0 = 5$ μm^{-1} and $k_{N\text{-}WASP} = 0.01$ μm/s.

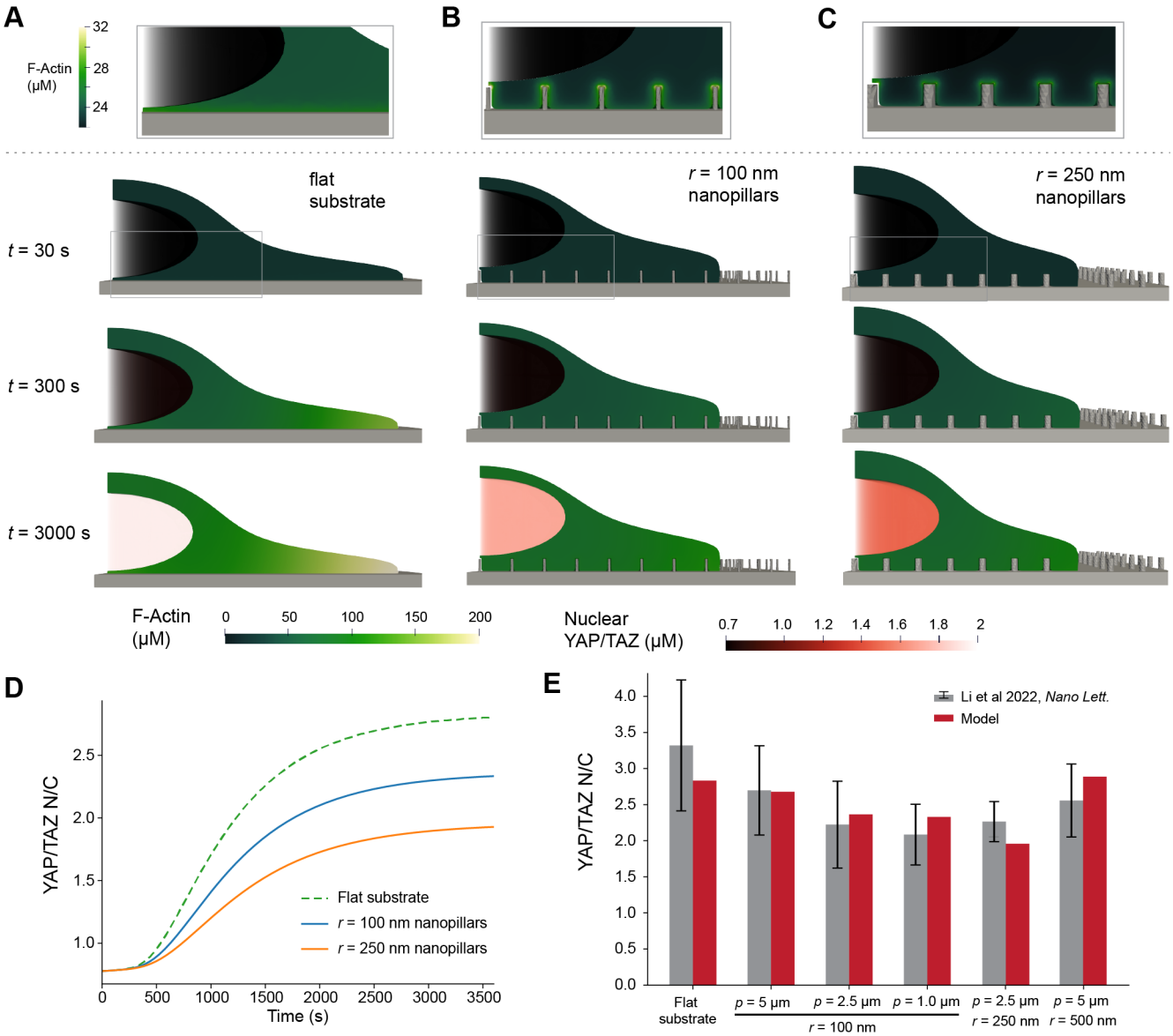

Figure 2: Simulations of nuclear translocation of YAP/TAZ on nanopillar substrates agree with experimental measurements. A-C) Spatial distributions of cytosolic F-actin (green) and nuclear YAP/TAZ (red) at 3 different time points for model cells on a flat substrate (A) or substrates with nanopillars of radius 100 nm (B) or 250 nm (C). Both nanopillar substrates share the same height (1 μm) and spacing (2.5 μm) of nanopillars. Upper insets show a magnified snapshot of the F-actin distribution around individual nanopillars or above the flat substrate at t = 30 s using a different color scale. D) YAP/TAZ N/C dynamics for the three cases shown in A-C. E) Steady-state YAP/TAZ N/C for several nanopillar substrates tested in [8], compared to those predicted by our best-fit model where $H_0 = \mu m^{-1}$ and k_{WASP} = 0.01 μm/s. Experimental data is reported as mean ± standard deviation from Fig S10 in [8]. From left to right, N = 396, 38, 89, 59, 58, and 48.

Nanopillar-induced nuclear deformation leads to increases in the stretch and curvature of the nuclear envelope

Our previous studies showed that the nuclear size and shape influence YAP/TAZ N/C ratio independently of global cell shape [20]. As previous studies have measured large deformations of the nucleus on nanopillar substrates [12, 30], we aimed to determine the extent of nuclear deformation by measuring nuclear indentation and NE curvature in spread U2OS cells on nanopillar substrates.

In our experiments, cells were seeded on nanopillar substrates with base diameter 1.17 ± 0.39 μm, center-to-center pitch 3.50 ± .08 μm, height 3.33 ± 0.21 μm, and tip diameter= 0.4 ± 0.0554 μm (all reported as mean ± standard deviation). The U2OS nuclei were dramatically deformed, exhibiting indentations up to 3.5 μm in certain cases (Figure 3A-B). The curvature induced by such deformations ranged from 2.5-4.5 μm^{-1} (Figure 3B).

We reproduced these nuclear deformations in our model by defining a deformation field on the surface of an ellipsoidal nucleus (Figure 3C-F). For simplicity, we assumed that material points were displaced mainly in the vertical (z) direction due to the nanopillar-induced stress. The resulting area stretch ratio (area dilation) and curvature of the nuclear surface could then be directly calculated (Supporting Information, Section S5). Regions of highest stretch were localized to the nuclear membrane adjacent to the sides of the nanopillars, while the top surface remains unstretched (Figure 3D,F). Importantly, these stretch ratios should not be taken to correspond to areal dilation of the nuclear membrane itself, but rather the elastic stretching of the underlying nuclear lamina [31]. The spatially resolved curvatures match expected values; for instance, mean curvature of the nuclear membrane adjacent to nanopillars is close to the mean curvature of nanopillar sides themselves (1 μm^{-1}). The spatially averaged mean curvature agrees well with experimental measurements - H_{PM} averaged over the membrane indented by the central nanopillar in Fig 3F is 3.4 μm^{-1}.

Nuclear indentation enhances cytoskeletal activation and allows for increased YAP/TAZ transport through NPCs

We next measured the distribution of F-actin (Fig 4A) and Lamin A/C (Fig 4B) in U2OS cells on nanopillars. We used an 8-hour time point to allow cells to adhere and spread on nanostructures. The focal plane was carefully chosen to ensure optimal visualization of the cellular structure and fluorescence images were taken which showed accumulation of F-actin around the nanopillars, in agreement with previous studies [6, 11]. These sites of actin accumulation were mainly observed near the center of the cell body, likely near regions of nuclear indentation. Lamin A/C also appeared to concentrate around nanopillars, which is at least in part attributed to a greater density of NE surface projected to the focal plane in cases of nuclear deformation.

We then simulated the predicted effects of nuclear deformation on cytoskeletal activity and lamin phosphorylation in our computational model. Due to N-WASP-mediated actin polymerization near the surface of the nanopillars and the effects of confinement between the PM and NE, we observed a higher concentration of actin surrounding nanopillars in the region of nuclear deformation (Figure 4C). For comparison with experimental images, we computed the projected density of F-actin at $z = 2$ upon convolution with a Gaussian kernel for a cell at steady-state (see Methods, Equation (6)). This intensity map qualitatively matched experimental measurements (Figure 4A,C). Similarly, we examined the effects on lamin distribution, as indicated by the surface density of dephosphorylated lamin A. In accordance with model assumptions, lamin A is preferentially dephosphorylated in regions with higher concentrations of F-actin, leading to higher concentrations near sites of nuclear indentation here (Figure 4D). Once again, we computed the intensity projection onto the $z = 2$ plane, revealing a distribution quite similar to experimental measurements (Figure 3B,D). This local assembly of lamin A also agrees well with other measurements of lamin A distribution following cell deformation on nanoneedle substrates [32].

Next, we predicted the effects of nuclear indentation on transport of YAP/TAZ through NPCs. Lamin A dephosphorylation directly potentiates NPC opening in our baseline model. In addition, previous measurements show that stretching of the NE facilitates the opening of nuclear pore complexes (NPCs), allowing increased entry of YAP/TAZ and other factors [25, 27]. We then proposed the transport rate exponentially scaled with the the local stretch ratio α of the NE (Figure 4E):

$$k_{in,NPC} = (k_{inb} + k_{in}[NPC_A]) \exp\left(\frac{\alpha - 1}{\alpha_0}\right), \tag{3}$$

where k_{inb} and k_{in} are the basal and NPC-activation-dependent rates of YAP/TAZ transport into the nucleus,

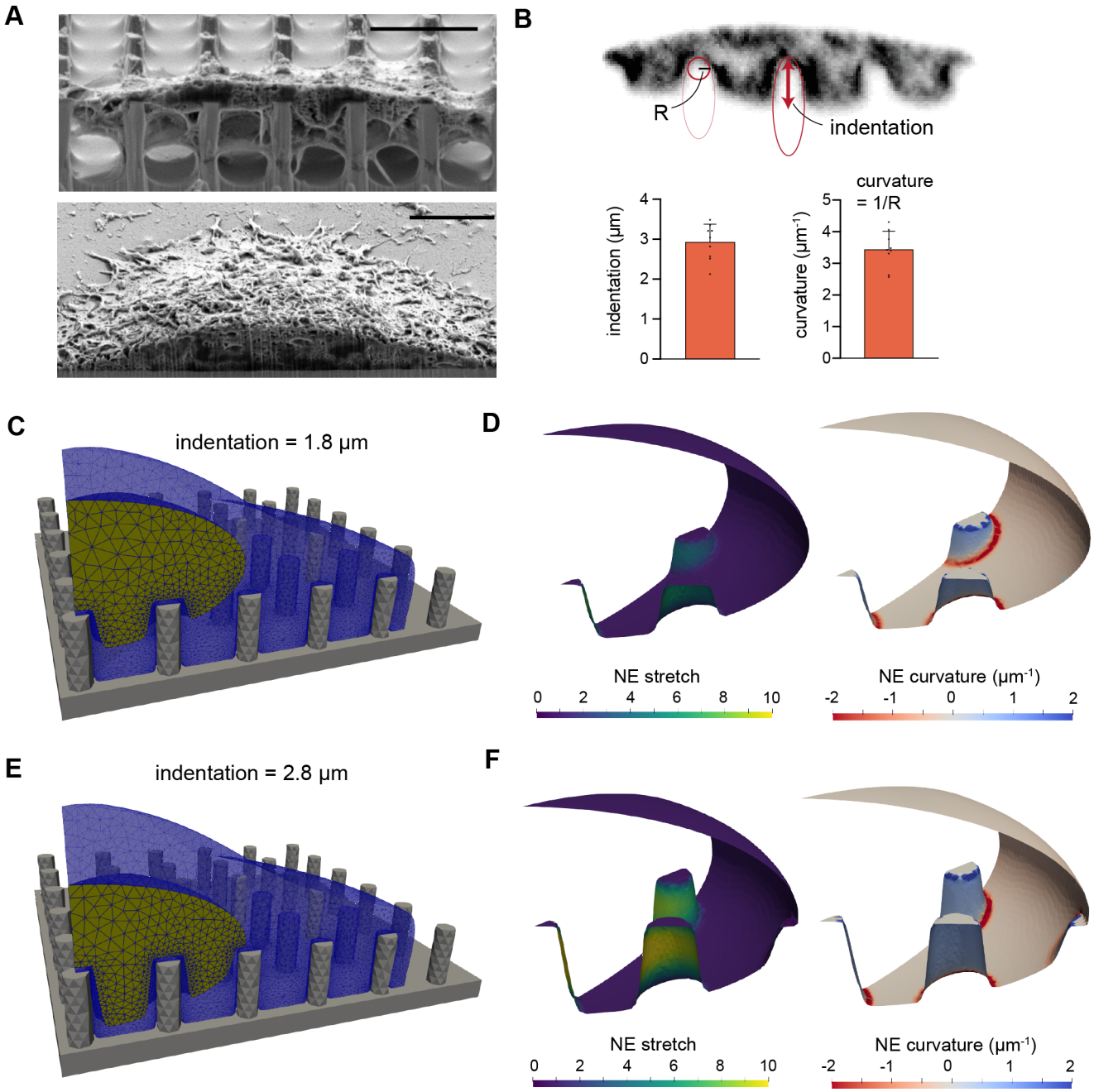

Figure 3: Plasma membrane nanotopography induces nanoscale curvature in the nuclear membrane. A) Cross-sectional images of spread U2OS cells on a nanopillar substrate (upper) and flat surface (lower) using Focused Ion Beam Scanning Electron Microscopy. Scale bar denotes 5 μm. B) Quantification of nuclear indentation and NE curvature from reconstructed confocal microscopy images. The circle of radius R and elongated ellipse represent the shapes drawn to quantify NE curvature and indentation, respectively. $N = 9$ in bar graphs. C-F) Meshes of model cells on substrates with $r_{NP} = 500$ nm, $h_{NP} = 3$ μm, $p_{NP} = 3.5$ μm and nuclear indentations of 1.8 μm (C) or 2.8 μm (E). Calculated NE stretch (Eq S46) and NE curvature (Eq S49) are displayed for each mesh in D and F.

respectively, $[NPC_A]$ is the surface density of activated NPCs and α_0 sets the sensitivity of NPC transport to stretch. According to this equation, entry is enhanced in regions of stretch ($\alpha > 1$) and reduced in regions of compression ($\alpha < 1$).

For large indentations of the NE, this leads to faster entry of YAP/TAZ at regions of high stretch. Examining the model across a range of nuclear indentations, we observed distinct elevations in N/C YAP/TAZ ratio for increased indentation when α_0 is less than or equal to 5 (Fig 4F, Movies 7 to 10). In the absence of stretch sensitivity, the model surprisingly predicts reduced YAP/TAZ N/C at high levels of nuclear indentation. We found that this can be attributed to a reduced gap between the nucleus and PM at the top of the cell geometry (Figure S2, Movie 7). In subsequent simulations, we fixed the stretch sensitivity at $\alpha_0 = 5$, as this value predicts a substantial increase in YAP/TAZ N/C with nuclear indentation without predicting values of YAP/TAZ N/C much higher than most experimental measurements. Enhanced entry of YAP/TAZ at regions of high stretch, together with N-WASP-mediated actin assembly at closely apposed regions of PM, may compensate for weakened mechanosignaling due to endocytosis.

Nuclear rupture leads to high levels of YAP/TAZ in select cells on nanopillar substrates

In addition to the effects of NPC stretch due to nanopillar-induced deformation of the NE, recent experiments indicate that some cells seeded on nanopillar substrates experience transient NE rupture (NER) [12]. This was shown to cause a protein normally confined to the nucleus, Ku-80, to escape into the cytosol. We postulated that a similar effect might hold true for YAP/TAZ; that is, NER might allow for increased nuclear entry and/or exit of YAP/TAZ (Figure 5A). Unlike NPC-mediated transport, the movement of YAP/TAZ through rupture-induced pores may not be sensitive to YAP phosphorylation state - phosphorylated YAP/TAZ, normally confined to the cytosol, would be allowed to enter the nucleus through such pores. Furthermore, rupture-induced pores may not exhibit the same directional selectivity as NPCs; that is, entry and exit of certain proteins could occur at similar rates.

We therefore included an additional entry mechanism over a small patch of the nuclear surface designated as a rupture-induced pore in some simulations. We consider a pore that opens rapidly at the central nanopillar, which we represent implicitly through an spatiotemporal function defining the relative permeability p of the NE (Figure 5B):

$$p_{NER} = \left(1 - \exp\left(-\frac{t}{t_0}\right)\right) \exp\left(-\frac{x^2 + y^2 + (z - z_{NE})^2}{\sigma_{pore}^2}\right), \tag{4}$$

where σ_{pore} dictates the size of the pore, t0 represents the time-scale of pore formation, and z_{NE} is the z value associated with the lower portion of the NE at $x = 0$, $y = 0$. Here, we assume that the pore forms rapidly ($t_0 = 1$ s), in line with previous measurements of PM damage [33].

The entry and exit rates of molecules through this pore are given by:

$$\begin{aligned} k_{in,rupture} &= \upsilon k_{rupture} p \\ k_{out,rupture} &= k_{rupture} p, \end{aligned} \tag{5}$$

where υ represents the ratio of the two rates of transport (entry/exit ratio) and $k_{rupture}$ sets the magnitude of the transport rates.

To test the effects of entry rate and rupture-induced pore size in our model, we systematically varied $k_{rupture}$, υ, and σ_{pore}. Increasing $k_{rupture}$ and/or σ_{pore} alters the contribution of transport through the rupture-induced pore relative to transport through NPCs, whereas υ determines the extent to which YAP/TAZ movement is biased inward vs. outward. When $\upsilon = 5$, NE rupture caused increases in nuclear YAP/TAZ compared to conditions without rupture (Figure 5C,E, Movie 11). The extent and rate of this increase depends on the overall transport rate (the product of the pore surface area and $k_{rupture}$). However, we found that when $\upsilon = 1$, YAP/TAZ N/C is lower than the baseline condition, as entry and exit through the pores occur at similar rates (Figure 5D-E, Movie 12).

We noted that spatial gradients in YAP/TAZ throughout the cytosol and the nucleus were relatively small; that is, YAP/TAZ was generally well-mixed in these simulations. In fact, we found that our spatial model results agree well with a well-mixed model of YAP/TAZ transport (Figure S3). Accordingly, we were able to sweep across a wide range of transport rates and entry/exit ratios without computing all individual cases using the full spatial model

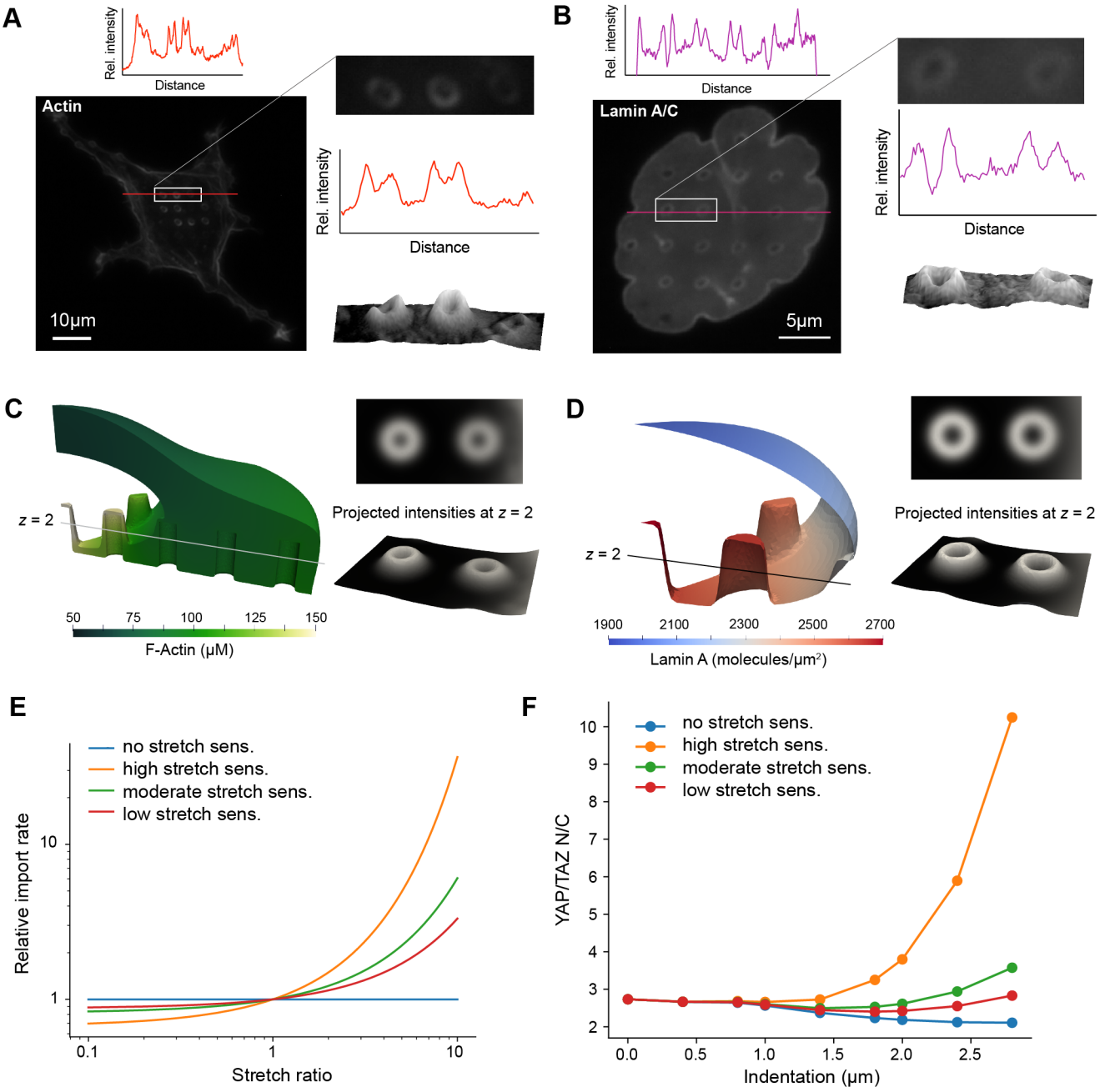

Figure 4: Effects of nuclear indentation on cytoskeletal activation, lamin organization, and nuclear transport. A) Fluorescence images of actin in a U2OS cell, with an intensity profile quantified along the red line. The right images show a magnified image of actin accumulation around 3 nanopillars, with the associated intensity profile (middle) and surface plot (lower). B) Fluorescence image of lamin A/C localization in a region of nuclear deformation on nanopillars, with the associated intensity profile along the red line. The right images show a magnified image of lamin intensity around 2 nanopillars, with the associated intensity profile (middle) and surface plot (lower). C) Actin distribution in a model cell at t = 10,000 s, with right images showing the projection to the $z = 2$ plane for comparison with fluorescence images. D) Distribution of non-phosphorylated lamin A in the NE at t = 10,000 s, with right images showing projected intensities at the $z = 2$ plane. E-F) Exponential relationship between import rate through NPCs and the stretch ratio (area dilation) of the NE for different values of α_0 (E) and the resulting steady-state YAP/TAZ N/C for different levels of nuclear indentation (F).

(Figure 5F). When υ is greater than about 3.5, our model predicts accumulation of YAP/TAZ at steady-state, with larger relative increases associated with larger pores or faster transport.

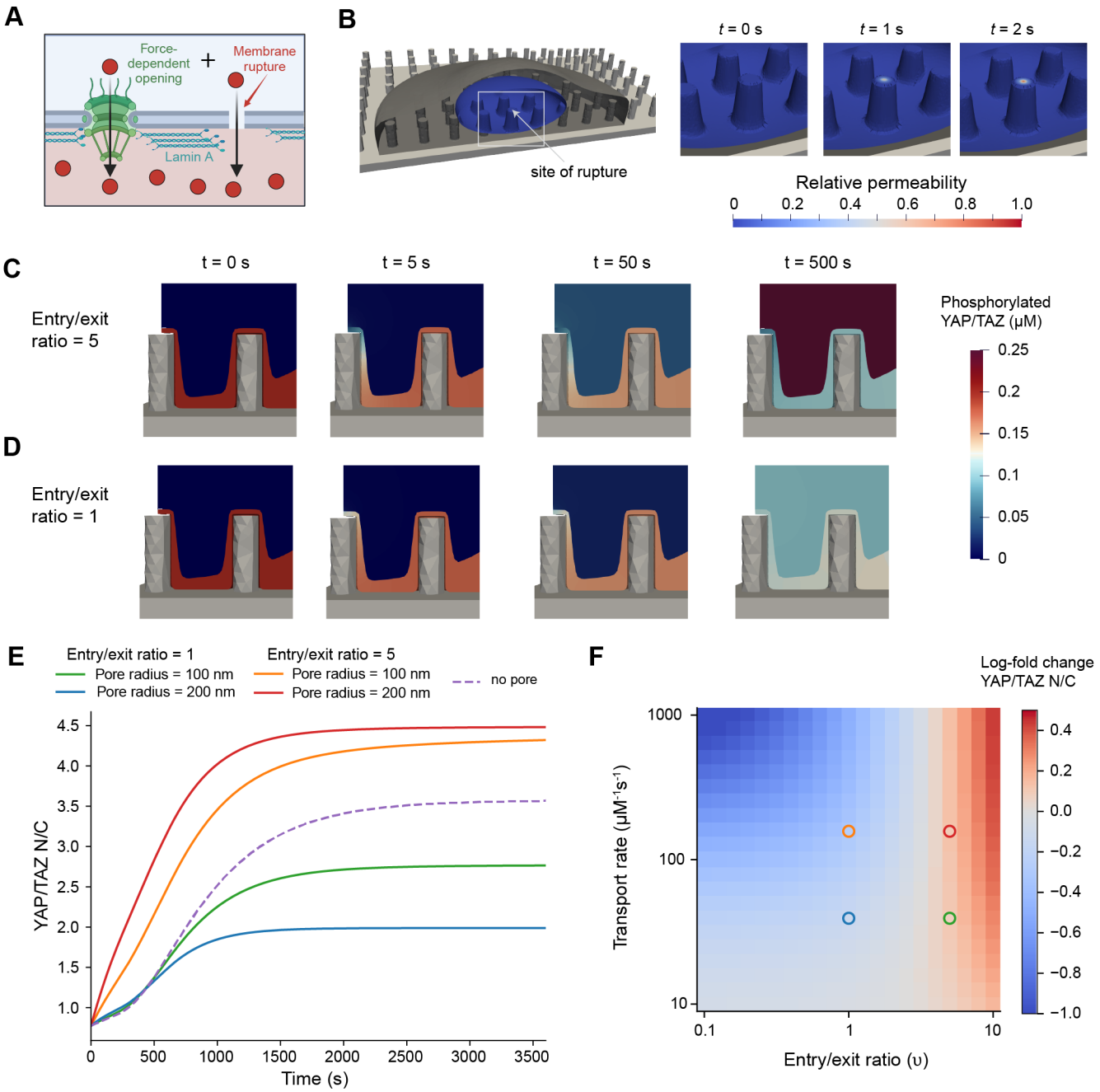

Figure 5: Model predicts changes in nuclear YAP/TAZ following rupture of the nuclear envelope. A) Schematic depicting the combination of force-dependent NPC opening and molecular transport through NE rupture-induced pores. B) Example sequence of pore formation at the nuclear membrane positioned above the central nanopillar for σ_{pore} = 0.2 μm and t_0 = 1 s in the model cell with nuclear indentation of 2.8 μm. C-D) Spatial distributions of phosphorylated YAP/TAZ in the cytosol and nucleus for an entry/exit ratio (υ) of 5 (C) or 1 (D). Both cases begin with no phosphorylated YAP/TAZ in the nucleus and exhibit local depletion of phosphorylated YAP/TAZ in the cytosol near the site of pore formation. E) Dynamics of YAP/TAZ N/C for different pore radii (100 nm or 200 nm) and different entry/exit ratios (1 or 5), compared to simulations with no pore (dashed line). In C-E, krupture was fixed at 10,000 $\mu m^{-2} s^{-1} \mu M^{-1}$. F) Phase diagram showing the (base-10) log fold-change YAP/TAZ N/C at t = 3600 s as a function of entry/exit ratio (υ) and transport rate ($\pi \sigma_{pore}^2 k_{rupture}$) with respect to the case of no NE rupture. The individual points mark the cases plotted in panel E, with edge color corresponding to their line color in the first plot.

To test these model predictions, we examined the YAP N/C for cells on nanopillars in our experiments. As recently

reported [12], some cells did show evidence of NER, indicated by the cytosolic mislocalization of Ku-80, a molecule normally localized to the nucleus (Figure 6A). Concurrently, we observed an increase in nuclear localization of YAP molecules in the same cells (Figure 6A). We then examined the average behavior over many cells, defining cases of NER as those cells with Ku-80 cytosolic-to-nuclear ratios greater than 0.16. In agreement with previous studies [8, 34], our quantitative analysis confirmed that, among cells not experiencing NER, those on flat substrates exhibited significantly higher YAP N/C ratio compared to those on nanopillars (Figure 6B). Additionally, cells exhibiting NER had a significantly elevated YAP N/C ratio compared to cells on nanopillars without rupture (Figure 6B), suggesting NER enhances the translocation of YAP to the nucleus. This is further supported by the statistically significant positive correlation between the cytosolic-to-nuclear Ku-80 ratio and YAP N/C for cells on nanopillar substrates (Figure 6C).

In relation to our model, this data indicates that transport of YAP through rupture-induced pores is still directionally biased; that is, the rate of import is greater than the rate of export. Overall, we find that our model best matches experiments for rapid rates of transport through rupture-induced pores with a significant bias towards inward transport (towards the top right of the phase diagram in Figure 6F). Together, our experiments and simulations position NER as an additional pathway for molecular transport across the NE in response to substrate topography.

Discussion

Mechanotransduction, the process of cell signaling in response to mechanical cues, is a key regulator of cell state, proliferation, and differentiation [35]. One of the key mechanical cues is the local stiffness in the pericellular microenvironment that regulates how cells can sense their immediate environment [20, 22]. Our findings highlight the additional importance of ECM topography in cell mechanosignaling. Many recent experiments demonstrate the importance of nano-scale topographical cues to local cytoskeletal assembly [5, 6, 10], endocytosis of PM proteins [7, 8], and deformations of the NE [12, 30, 34], each of which have significant downstream effects on the nuclear translocation of YAP/TAZ. However, our computational model is the first to incorporate these effects into a predictive computational model of cell mechanosignaling. Our findings reveal that cell signaling integrates many mechanical and geometric cues including PM curvature, cytoskeletal assembly, and nuclear mechanics, resulting in mechanoadaptation.

Many previous models of YAP/TAZ mechanotransduction assume the cell to be a composite of well-mixed volumes [19, 21, 36]. This results in a system of ordinary differential equations (ODEs), which is not generally equipped to handle the complex dynamics of signaling networks in realistic cell geometries. Other recent models consider the spatial dynamics of mechanotransduction [20, 23, 37, 38], but these simulations were restricted to relatively simple model geometries. Here, we consider detailed cell geometries on several different nanopillar substrates, making use of our new software package, SMART [23, 24], which is especially well-suited for simulating detailed cell geometries. While spatial considerations are indispensable for many features of our model, in certain cases a well-mixed treatment can still be justified, significantly reducing computational cost. For instance, we modeled the YAP/TAZ species as a well-mixed subset of our system while retaining reasonable agreement with full spatial simulations (Figure S3). This permits parameter sweeps (e.g., Figure 5F) that could otherwise be computationally prohibitive.

Extrapolating from past modeling work, the effects of surfaces such as nanopillars on mechanotransduction remained unclear. On one hand, cells on substrates with nanoscale curvature have increased PM surface area to cytosolic volume ratios, a condition in which previous models and data suggest that cytoskeletal activation and YAP/TAZ nuclear translocation are enhanced [20, 23, 39]. In contrast, experimental data seems to suggest that signaling is attenuated on nanopillar substrates due to enhanced endocytosis of integrins [8]. Our spatial simulations establish that this phenomenon can be sufficiently represented by curvature-dependent inhibition of FAK phosphorylation. This effect persisted even when allowing for local polymerization of actin at sites of high curvature, representing a delicate balance between local activation and global inhibition reminiscent of putative models for cell navigation in response to chemical gradients [40, 41]. Similarly, the mechanoadaptation described by our model may be well-suited to steer cell migration through complex topographies.

The mechanisms of molecular transport through rupture-induced pores in the NE remain unclear. Here, we use simple empirical relationships to model fluxes through these pores, assuming that YAP/TAZ phosphorylation state does not influence the entry/exit rates and that the entry and exit rates could be different from one another. While transport through NPCs has been clearly demonstrated as directionally biased [42], one might naively assume that fluxes through rupture-induced pores could be purely passive, modeled as a Fickian flux (that is, $\upsilon = 1$ in Equation (5)). However, this assumption is clearly at odds with our experimental data, as demonstrated in Figures 5 and 6. This

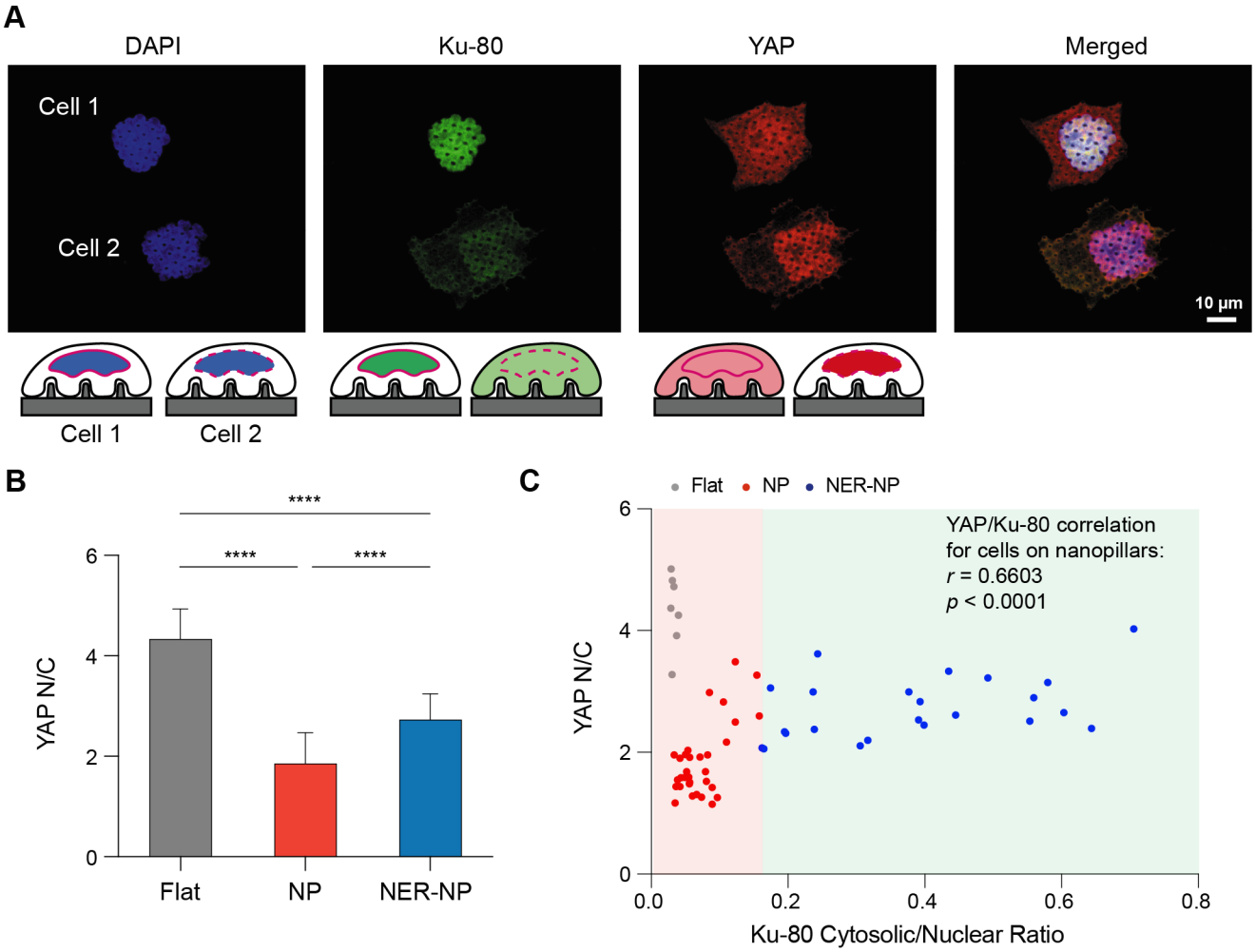

Figure 6: YAP localizes to the nucleus upon nuclear envelope rupture. A) Immunofluorescence imaging of cells stained for nuclear location (DAPI), NE rupture marker (Ku-80), and YAP demonstrate the the localization of Ku-80 to the nucleus and uniform distribution of YAP signal in whole cell (cell 1) where cell 2 shows mislocalization of Ku-80 from nuclear region to the cytoplasmic region and localization of YAP molecules to the nuclear area. Scale bar denotes 10 µm. B) Quantitative comparison of YAP nuclear/cytoplasmic ratio of cells on flat, NP, and NER-NP substrate reveals higher translocation of YAP to the nucleus on the ruptured cells compared to the NP area. ****$p < 0.001$ according to two-way ANOVA. C) Scatter plot illustrating the positive correlation between YAP N/C and Ku-80 cytosolic/nuclear ratio as nuclear envelope rupture where cells in rupture state show an elevated YAP N/C. Correlation was assessed between YAP N/C and Ku-80 cytosolic/nuclear ratio for all measured cases of cells on nanopillars (both NP and NER-NP). r denotes Pearson's correlation coefficient and p is the p-value associated with the null hypothesis $r = 0$. In B and C, $N = 7$ for cells on a flat substrate, $N = 32$ for cells on nanopillars with no NER, and $N = 23$ for cells on nanopillars with NER.

could likely be attributed to YAP/TAZ undergoing some additional chemical modification or binding event following transport into the nucleus that does not allow for its movement back into the cytosol. For instance, YAP/TAZ could rapidly form a complex with TEADs and/or chromatin, slowing or halting their diffusion and lowering the probability of passing back through a small membrane pore. In the rapid-binding limit, this would appear identical to the case in which the exit rate is much slower than the entry rate. We also assumed that NER does not impact the distribution of other signaling components included in our model. However, many of these cytosolic proteins are comparable in size or even smaller than YAP and TAZ, and they may in fact be able to pass through these pores. Finally, although we assume that the pore remains open over extended times in our model, membrane repair may begin within a short time of the rupture event.

The process of NE rupture and nuclear membrane repair require additional consideration in future experiments and models. While we just recently reported such events in response to nanotopographical features [12], related transient changes in NE integrity have been observed in response to many different mechanical stimuli during cancer and immune cell migration [43, 44]. NE disruption is generally understood to be detrimental to cell function, associated with diseases such as laminopathies, cardiomyopathies, and cancer, or with cellular aging (senescence) [45, 46]. However, our findings suggest that at least some cases of temporary NE rupture can enhance cell mechanotransduction. Whether such responses are observed *in vivo* under non-pathological conditions remains to be seen.

N-WASP-mediated actin assembly around nano-curved surfaces, stretch-activated NPC opening, and rupture of the NE are all potential compensatory mechanisms for reduced signaling due to receptor endocytosis at sites of inward curvature [7, 8]. The contribution of each process to YAP/TAZ signaling depends on adjacency between the PM and NE (see Figure S2) and on the extent of nuclear deformation. These are generally controlled by the cell itself rather than any externally applied force. Experiments and models indicate that the nucleus is deformed due to combined effects of downward force of an "actin cap" pushing downward on the nucleus and to the anchoring of the lower NE to the PM [30, 47]. This process of nuclear deformation therefore effectively acts as an internal dial by which the cell can tune nuclear transport of YAP/TAZ. This may be especially important for cancer cells, such as the U2OS cells tested here, which were chosen due to their responsiveness to physical stimuli and mechanosensitive pathways common to many cancer cells [48, 49]. Changes in nuclear YAP/TAZ are a key determinant of differentiation and metastasis across many cancers [2, 50].

The curvature- and deformation-dependent signaling events explored in this paper apply well beyond YAP/TAZ mechanotransduction networks. First, the modulation of cytoskeletal assembly by PM curvature has implications for many cell responses to different nanotopographies, from immune cell migration [5] to alignment of fibroblasts along collagen fibrils [51]. Furthermore, the enhancement of endocytosis at sites of high curvature could have effects on many different signaling cascades initiated at the PM. Similarly, NPC stretching and NER could influence the transport of many different factors to and from the nucleus in addition to YAP/TAZ. Thus, the integration of mechanical and chemical cues at multiple length scales is critical for mechanoadapatation.

Methods

Mesh generation

All meshes were generated using the open-source mesh generator Gmsh [28]. For simplicity, we assume that nanopillar substrates are well-described by a composite of a flat surface and cylindrical structures of a specified height, spacing (pitch), and radius (cf. Figure 1B). Furthermore, our model cell geometries formed a circular contact area over the substrate, with one nanopillar positioned directly at the center of the contact region. In this case, the model geometry cell has four unique symmetry axes ($x = 0$, $y = 0$, $y = x$, and $y = -x$), allowing us to simulate 1/8 of the full geometry, saving computational cost. The PM closely conformed to the nanopillar surface, in agreement with experimental observations [30]. In particular, the PM was assigned to be 50 nm from the nanopillar surface in all locations except close to the lower flat substrate, where the membrane curved to smoothly meet the surface with a characteristic radius of 200 nm (Figure S4A, Eq S33). We prescribed the projected cell contact area according to experimental measurements for each condition, with the added constraint of conserved cell and nuclear volume matching previous measurements of U2OS cells [52]. All substrates were assumed to have a Young's modulus of 10 GPa.

The nuclear mesh was continuous with the cytosolic mesh, with its reference boundary specified as an oblate spheroid with aspect ratio 2.21:1 (Eq S5) and volume matching that measured in experiments with U2OS cells [52]. The bottom of the nucleus was positioned 0.2 μm above the PM at the central nanopillar. In cases where the top of the nucleus did not fit within 0.8 μm of the top PM boundary, the vertical axis length was reduced and the radial axis was

expanded to conserve volume (Eq S10-S11). In cases of nuclear deformation, the nuclear boundary was modified in Gmsh according to Eq S41.

A summary of geometric parameters, volume and area of each subsurface and subvolume, and number of nodes and elements in each subsurface and subvolume are given for each mesh in Table S1. Meshes used in the final simulations are freely available via Zenodo [53].

Spatial simulations of YAP/TAZ signaling

All simulations were conducted using the Python package, Spatial Modeling Algorithms for Reaction and Transport (SMART), recently developed by our group [23, 24]. The SMART framework takes in user specifications of the species, reactions, parameters, and compartments involved in a given reaction-transport network. Our model involves 16 species across four compartments: the plasma membrane, the cytosol, the nuclear envelope, and the nucleoplasm (Table S2). All reactions between species and parameters governing these reactions are summarized in Tables S3-S4. Other than the equations given in the main text, all reactions were used as specified in previous work [20, 23].

These specifications, together with diffusion coefficients and initial conditions for each species, define the system of nonlinear mixed dimensional PDEs governing the system (Eqs S14-S28). SMART internally expresses these equations in their variational form and assembles a monolithic finite element system using the finite element software FEniCS. We use linear finite element shape functions for each triangular or tetrahedral element and discretize in time according to a backward (implicit) Euler scheme. The nonlinear system is solved at each time step using Newton-Raphson iterations in PetSc [54]. We chose an initial time step of 0.01 s, after which SMART adaptively adjusted the time step according to the number of Newton iterations required for convergence at the previous time. Our code for model specifications, mesh creation, and data analysis is freely available on Github [55]. Results files are also available via Zenodo [53]. All visualization shown in figures and videos was conducted in Paraview.

Computation of projected intensity maps from simulation data

For comparison with experimental images, we computed a projection of our finite element solution onto the z = 2 plane in Figure 4. To compute this, we convolved our spatial solution with a Gaussian kernel; that is, the projected intensity I was given by:

$$I(x,y,z) = \frac{1}{\sigma_x \sigma_y \sigma_z \pi^{3/2}} \int_{\Omega} c(\xi,\psi,\omega) \exp\left(-\left(\frac{\xi - x}{\sigma_x}\right)^2 - \left(\frac{\psi - y}{\sigma_y}\right)^2 - \left(\frac{\omega - z}{\sigma_z}\right)^2 \right) d\Omega, \tag{6}$$

where $c(x,y,z)$ is the spatially defined finite element solution (either for lamin A or F-actin in this context), and $\sigma_x = \sigma_y = 0.2$ µm and $\sigma_z = 0.4$ µm to represent the effects of blurring in the x-y plane vs. blurring in the z direction. This mimics the effect of convolution with the point spread function (PSF) to compute an image in optics. Here, we use a simpler functional form than a conventional PSF as our comparison with fluorescence images is purely qualitative.

Nanopillar substrate fabrication and preparation

Nanopillars were fabricated as previously described [56]. Briefly, quartz wafers were cleaned and spin coated with AZ 1512 photoresist (EMD Performance Materials) with 1.2 µm thickness. Patterning and exposure were performed using the Heidelberg maskless aligner (MLA) with a 375 nm laser at 300 mJ/cm^2. Chromium (Cr, 99.998%) was deposited using the Temescal Ebeam Evaporator, followed by lift-off. Reactive ion etching (RIE) with Ar and CHF_3 gases was performed over a 50-minute process using the Oxford Plasmalab 80plus. Finally, wet etching with Cr etchant (Transene Company Inc) and BOE 20:1 completed the fabrication, and the wafers were diced into 1 cm^2 chips for further experimentation. Chips were sterilized with 70% ethanol, rinsed with deionized water, and air-dried. They were then UVO-treated for 10 minutes and incubated with 100 µg mL^{-1} poly-L-lysine (PLL) solution for 30 minutes. After washing with PBS, the chips were treated with 0.5% glutaraldehyde for crosslinking, followed by another PBS wash. Finally, a pre-warmed 0.1% gelatin solution was applied, and the chips were incubated at room temperature for 30 minutes.

U2OS cell experiments

U2OS (ATCC) were cultured in McCoy's 5A medium (ATCC) supplemented with 10% fetal bovine serum (FBS, Invitrogen) and 1% penicillin-streptomycin (PenStrep, Thermo Fisher Scientific) and were incubated at 37°C with 5% CO_2. Cells were seeded onto nanopillar chips by first detaching them with TrypLE Express Enzyme (Gibco) and preparing a 100 µL suspension containing 50,000 cells. After allowing 10 minutes for cell adhesion, 1 mL of growth medium was added to the 24 well-plate, and the cells were incubated at 37°C for further analysis.

Immunostaining

Cells were fixed after 8 hours of incubation using 4% paraformaldehyde (Electron Microscopy Sciences) at room temperature for 10 minutes. Then cells were permeabilized with Triton X-100 (Sigma-Aldrich, USA) for 10 minutes and blocked in 1% Bovine Serum Albumin (BSA) (Thermo Fisher Scientific) overnight before immunostaining. Rabbit anti-Ku-80 (Cell Signaling) at 1:200 dilution and mouse Anti-YAP1 Antibody (63.7) (Santa Cruz Biotechnology) at 1:100 dilution in PBS were used for primary antibody staining overnight at 4°C. Samples were washed 10 times with PBS to remove all primary antibodies. Samples were then incubated with secondary antibodies conjugated with Alexa Fluor 488 (anti-rabbit IgG, Thermo Fisher Scientific) or Alexa Fluor 594 (anti-mouse IgG, Thermo Fisher Scientific) at 1:1000 dilution for 1 hour at room temperature. Samples were washed in PBS and stained with 4′,6-diamidino-2-phenylindole (DAPI) (Thermo Scientific, USA) for 5 minutes. For the actin- and lamin-labeled cells shown in Fig 4, the same protocol was utilized, instead using a single primary antibody (mouse anti Lamin A/C from Biolegend at 1:400 dilution) and a single secondary antibody (anti-mouse IgG conjugated with Alexa Fluor 647 at 1:1000 dilution), followed by staining with Alexa 594-phalloidin (InvitrogenTM, USA) for 20 minutes.

FIB-SEM

Cell samples were prepared for SEM imaging by fixation in 2.5% glutaraldehyde overnight at 4°C, followed by three PBS rinses. Samples were dehydrated using ethanol with a series of 30%, 50%, 70%, 80%, 90%, and 100% with 10 min per step. Then samples were treated with Hexamethyldisilazane (HMDS) for 15 min and air-dried overnight. Samples were sputter-coated with iridium oxide, mounted on SEM stubs, and introduced into an FEI Scios DualBeam system (FIB/SEM). Cross-sectioning was performed using a 5 nA ion beam, with final cleaning at 0.5 nA. High-resolution images were acquired at 5 kV using an Everhart-Thornley Detector (ETD) to observe nanopillar-NE interactions.

Fluorescence microscopy

Widefield fluorescence images were captured using an Echo Revolve microscope equipped with a 40× Plan Fluorite LWD CC objective (NA 0.60). Confocal imaging was performed on a Nikon AXR microscope with a four-line laser system (405, 488, 561, and 640 nm) mounted on a Nikon Ti2 platform. Image stacks were captured in galvano mode with unidirectional scanning. z-stacks were acquired with 0.175 µm steps to capture the whole cell.

Image analysis

We utilized ImageJ version 1.53 (National Institutes of Health, USA) for image analysis. To quantify curvature, confocal images were reconstructed from side views using the reslice feature of ImageJ software. The largest fitting ellipse was manually drawn in an indented region of the nucleus, and the radius of a fitting circle tangent to the upper portion of this ellipse was calculated using ImageJ software (Figure 3B). The nuclear indentation was defined as the distance from the top of the ellipse to its center (Figure 3B).

To assess NE rupture and YAP localization, immunofluorescence staining was used to distinguish between nuclear and cytoplasmic regions, with the nucleus defined using a threshold based on the DAPI channel. Ku-80 and YAP intensity was measured within these nuclear boundaries, and cytoplasmic intensity was quantified in areas outside the nucleus but within the cell borders. Line profile analysis was performed using the "Plot Profile" function and surface profile analysis using the "Surface Plot" function in ImageJ.

Statistical analysis

For statistical analysis, we used GraphPad Prism (v9, GraphPad Software). Data for YAP nuclear to cytoplasmic ratio were analyzed using two-way ANOVA.* denotes $p \leq 0.05$, ** denotes $p \leq 0.01$, and *** denotes $p \leq 0.001$.

Acknowledgements

The authors would like to thank Dr. Marie Rognes at Simula Research Laboratories for her support and advice throughout the development of SMART that led to these simulations. Support in code development for SMART and guidance for mesh generation via Gmsh was provided by Dr. Jørgen Dokken and Dr. Henrik Finsberg at Simula Research Laboratories. Simulation results presented in this paper benefited from the Triton Shared Compute Cluster at the San Diego Supercomputer Center [57].

This work was supported in part by the Wu Tsai Human Performance Alliance at the University of California, San Diego (to P.R.). E.A.F. is supported by the National Science Foundation under grant EEC-2127509 to the American Society for Engineering Education and by the Wu Tsai Human Performance Alliance. This work was performed in part at the San Diego Nanotechnology Infrastructure (SDNI) of UCSD, a member of the National Nanotechnology Coordinated Infrastructure, which was supported by the National Science Foundation (Grant ECCS-2025752). This work was in part supported by the Air Force Office of Scientific Research YIP award (Award Number: 311616-00001), the Cancer Research Coordinating Committee faculty seed grant, National Science Foundation (Grant DMR-2011924) to to Z.J, and National Science Foundation (Grant DMR-2011924) to Z.J and A.S.

Supporting Figures and Movies

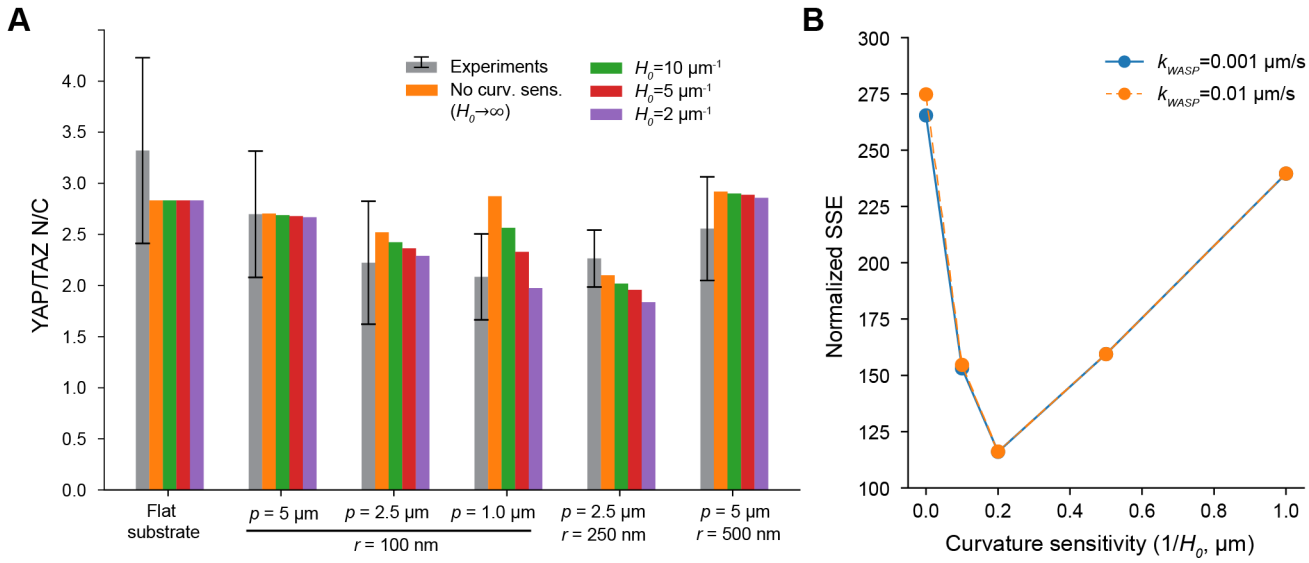

Figure S1: Determination of best-fit FAK curvature sensitivity. A) YAP/TAZ N/C in experiments (grey bars: mean ± standard deviation) and in simulations (spatially averaged at steady-state) with different levels of curvature sensitivity. B) Normalized SSE (Eq S9) as a function of curvature sensitivity ($1/H_0$) for two different rates of N-WASP-mediated actin assembly at regions of high PM curvature.

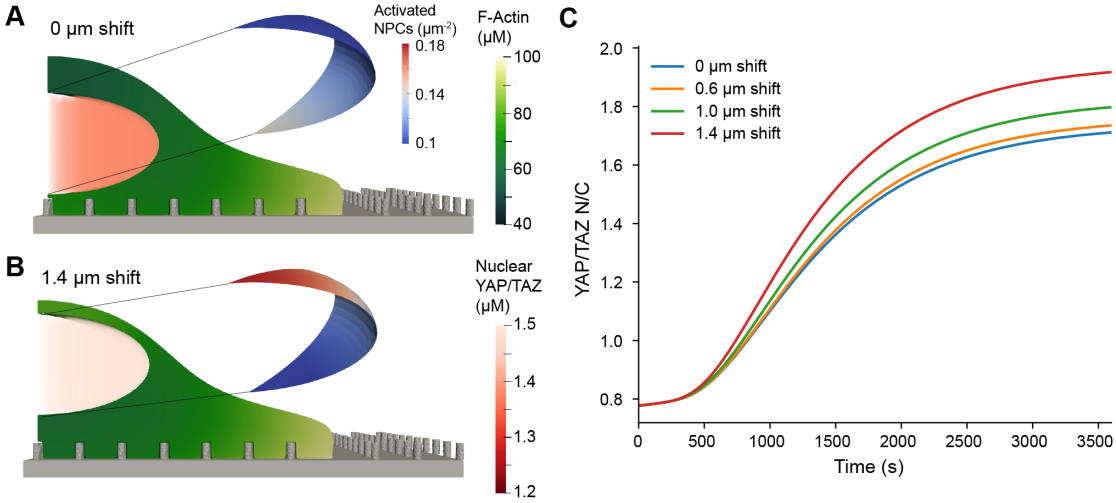

Figure S2: Decreasing the gap between the nucleus and upper plasma membrane enhances YAP/TAZ nuclear entry. A-B) Contrast in nuclear YAP/TAZ and F-actin distributions between the default nuclear position (A) and a nucleus shifted up by 1.4 μm (B) at steady-state (t = 10,000 s). In each panel, the inset shows the surface density of activated NPCs at the NE, revealing a high proportion of activation at the upper region of the nucleus in panel B. C) YAP/TAZ N/C dynamics for different nuclear locations, showing increased nuclear accumulation for larger vertical shifts. All simulations in this figure were conducted for a substrate with r_{NP} = 250 nm, p_{NP} = 2.5 μm, and h_{NP} = 1 μm.

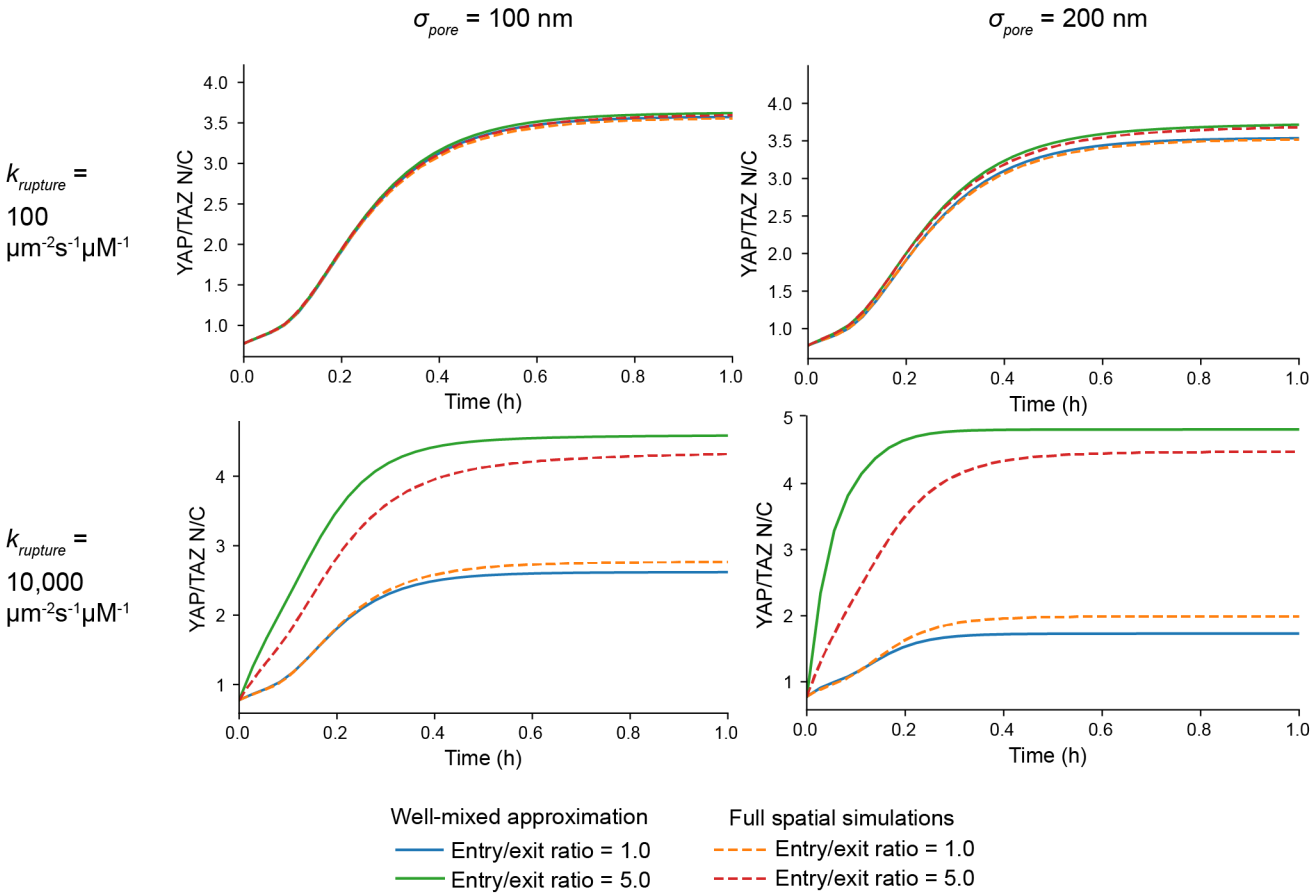

Figure S3: Well-mixed approximations match well with spatial simulations of YAP/TAZ transport. Comparison of YAP/TAZ N/C dynamics for slow entry through pores (upper plots) and fast entry through pores (lower plots), for two different pore sizes (100 nm and 200 nm radii) and two different entry/exit ratios (1.0 and 5.0). For slower transport, simulations show better agreement, whereas for rapid entry, spatial considerations significantly affect dynamics. However, in all cases tested here, the steady-state YAP/TAZ N/C predicted by a well-mixed model are within 15% of the spatial simulations.

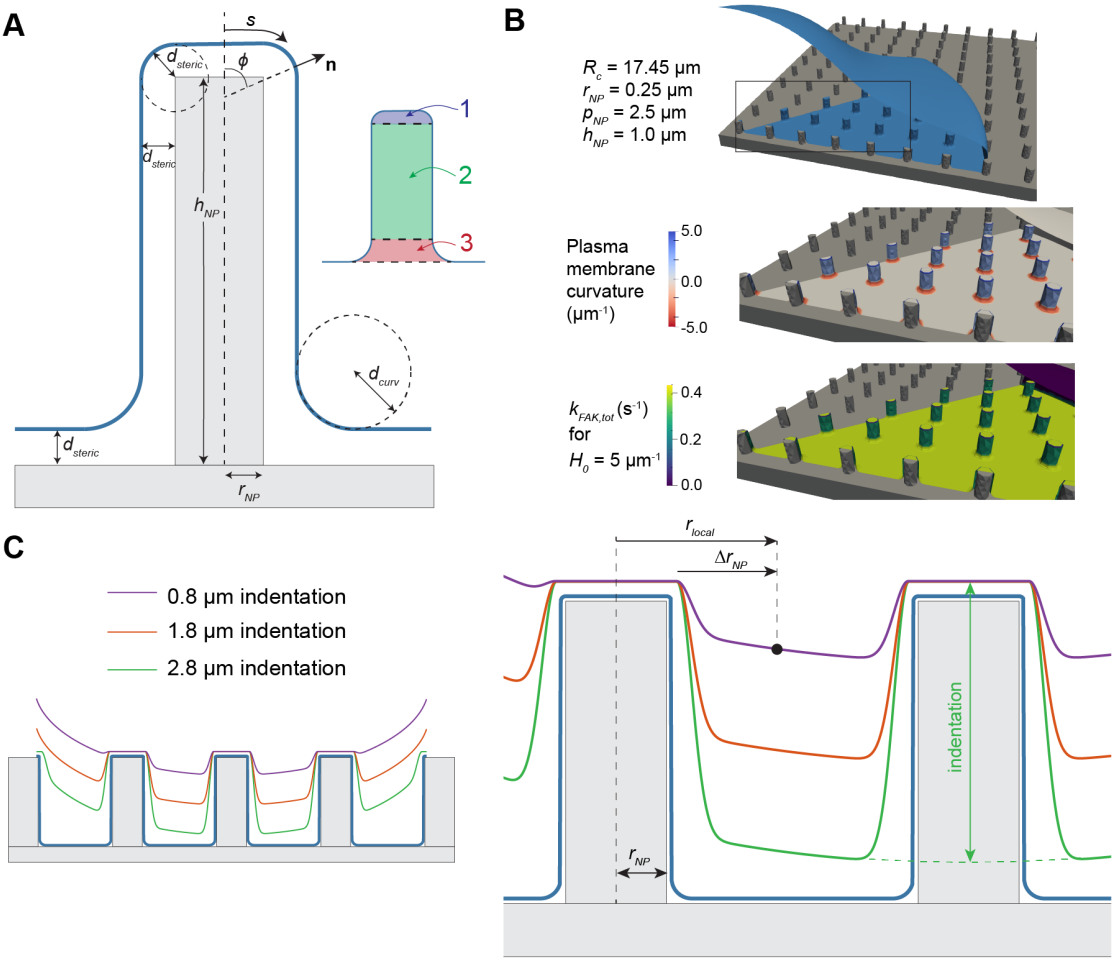

Figure S4: Schematics of plasma membrane and nuclear deformation on nanopillar substrates. A) Cross-section of the PM (blue) near the surface of a cylindrical nanopillar. Relevant parameters required for calculation of the PM curvature (Eq S35) are defined graphically. This section of the geometry is axisymmetric with respect to the axis defined by the dashed line. B) A sample PM geometry on a substrate with 250 nm radius nanopillars ($p_{NP} = 2.5$ µm, $h_{NP} = 1.0$ µm), along with the resulting PM curvature (middle) and the local rate of curvature-dependent FAK phosphorylation when $H_0 = 5\mu\text{m}^{-1}$ (lower). C) The $y = 0$ cross-section of prescribed deformations of the NE for different values of nuclear indentation. The substrate matches that shown in panel B. Inset here shows a magnified schematic with local coordinates (r_{local} and Δr_{NP}) defined with respect to the left nanopillar. PM configuration is plotted in blue.

Movie 1: Spatial dynamics of cytosolic F-actin and nuclear YAP/TAZ in a cell on a flat substrate (substrate stiffness = 10 GPa).

Movie 2: Fast time-scale dynamics of F-actin in a cell on a flat substrate (substrate stiffness = 10 GPa).

Movie 3: Spatial dynamics of cytosolic F-actin and nuclear YAP/TAZ in a cell on a substrate with 100 nm radius nanopillars (2.5 μm spacing, 1.0 μm height).

Movie 4: Fast time-scale dynamics of F-actin in a cell on a substrate with 100 nm radius nanopillars (2.5 μm spacing, 1.0 μm height).

Movie 5: Spatial dynamics of cytosolic F-actin and nuclear YAP/TAZ in a cell on a substrate with 250 nm radius nanopillars (2.5 μm spacing, 1.0 μm height).

Movie 6: Fast time-scale dynamics of F-actin in a cell on a substrate with 250 nm radius nanopillars (2.5 μm spacing, 1.0 μm height).

Movie 7: Spatial dynamics of cytosolic F-actin and nuclear YAP/TAZ in a cell on a substrate with 500 nm radius nanopillars (3.5 μm spacing, 3.0 μm height) with no nuclear indentation.

Movie 8: Spatial dynamics of cytosolic F-actin and nuclear YAP/TAZ in a cell on a substrate with 500 nm radius nanopillars (3.5 μm spacing, 3.0 μm height) with 0.8 μm nuclear indentation.

Movie 9: Spatial dynamics of cytosolic F-actin and nuclear YAP/TAZ in a cell on a substrate with 500 nm radius nanopillars (3.5 μm spacing, 3.0 μm height) with 1.8 μm nuclear indentation.

Movie 10: Spatial dynamics of cytosolic F-actin and nuclear YAP/TAZ in a cell on a substrate with 500 nm radius nanopillars (3.5 μm spacing, 3.0 μm height) with 2.8 μm nuclear indentation.

Movie 11: Spatial dynamics of cytosolic and nuclear phosphorylated YAP/TAZ following nuclear envelope rupture (pore radius = 200 nm) in a cell with 2.8 μm nuclear indentation, assuming entry/exit ratio (υ) = 5. The boundary of the nucleus is shaded to indicate NE permeability.

Movie 12: Spatial dynamics of cytosolic and nuclear phosphorylated YAP/TAZ following nuclear envelope rupture (pore radius = 200 nm) in a cell with 2.8 μm nuclear indentation, assuming entry/exit ratio (υ) = 1. The boundary of the nucleus is shaded to indicate NE permeability.

References

[1] Carlos F. Guimarães, Luca Gasperini, Alexandra P. Marques, and Rui L. Reis. "The Stiffness of Living Tissues and Its Implications for Tissue Engineering". In: *Nature Reviews Materials* 5.5 (Feb. 2020), pp. 351–370. ISSN: 2058-8437.

[2] LiKang Chin, Yuntao Xia, Dennis E Discher, and Paul A Janmey. "Mechanotransduction in Cancer". In: *Current Opinion in Chemical Engineering* 11 (Feb. 2016), pp. 77–84. ISSN: 22113398.

[3] Anna Yui and Madeleine J. Oudin. "The Rigidity Connection: Matrix Stiffness and Its Impact on Cancer Progression". In: *Cancer Research* 84.7 (Apr. 2024), pp. 958–960. ISSN: 0008-5472.

[4] Stephen F. Vatner et al. "Vascular Stiffness in Aging and Disease". In: *Frontiers in Physiology* 12 (Dec. 2021). ISSN: 1664-042X.

[5] Rachel M. Brunetti et al. "WASP Integrates Substrate Topology and Cell Polarity to Guide Neutrophil Migration". In: *Journal of Cell Biology* 221.2 (Dec. 2021), e202104046. ISSN: 0021-9525.

[6] Wei Zhang et al. "Curved Adhesions Mediate Cell Attachment to Soft Matrix Fibres in Three Dimensions". In: *Nature Cell Biology* 25.10 (Oct. 2023), pp. 1453–1464. ISSN: 1476-4679.

[7] Wenting Zhao et al. "Nanoscale Manipulation of Membrane Curvature for Probing Endocytosis in Live Cells". In: *Nature Nanotechnology* 12.8 (Aug. 2017), pp. 750–756. ISSN: 1748-3395.

[8] Xiao Li et al. "Nanoscale Surface Topography Reduces Focal Adhesions and Cell Stiffness by Enhancing Integrin Endocytosis". In: *Nano letters* 21.19 (Oct. 2021), pp. 8518–8526. ISSN: 1530-6984.

[9] Yang Yang et al. "Plasma Membrane Curvature Regulates the Formation of Contacts with the Endoplasmic Reticulum". In: *Nature Cell Biology* (Sept. 2024), pp. 1–14. ISSN: 1476-4679.

[10] Kexin Zhu et al. *Membrane Curvature Catalyzes Actin Nucleation through Nano-Scale Condensation of N-WASP-FBP17*. Apr. 2024.

[11] Hsin-Ya Lou et al. "Membrane Curvature Underlies Actin Reorganization in Response to Nanoscale Surface Topography". In: *Proceedings of the National Academy of Sciences* 116.46 (Nov. 2019), pp. 23143–23151.

[12] Einollah Sarikhani et al. "Engineered Nanotopographies Induce Transient Openings in the Nuclear Membrane". In: *Advanced Functional Materials* n/a.n/a (Sept. 2024), p. 2410035. ISSN: 1616-3028.

[13] Sirio Dupont et al. "Role of YAP/TAZ in Mechanotransduction". In: *Nature* 474.7350 (June 2011), pp. 179–183. ISSN: 1476-4687.

[14] Stefano Piccolo, Sirio Dupont, and Michelangelo Cordenonsi. "The Biology of YAP/TAZ: Hippo Signaling and Beyond". In: *Physiological Reviews* 94.4 (Oct. 2014), pp. 1287–1312. ISSN: 0031-9333.

[15] Xiaomin Cai, Kuei-Chun Wang, and Zhipeng Meng. "Mechanoregulation of YAP and TAZ in Cellular Homeostasis and Disease Progression". In: *Frontiers in Cell and Developmental Biology* 9 (May 2021). ISSN: 2296-634X.

[16] P P Provenzano, D R Inman, K W Eliceiri, and P J Keely. "Matrix Density-Induced Mechanoregulation of Breast Cell Phenotype, Signaling and Gene Expression through a FAK–ERK Linkage". In: *Oncogene* 28.49 (Dec. 2009), pp. 4326–4343. ISSN: 0950-9232, 1476-5594.

[17] M B Calalb, T R Polte, and S K Hanks. "Tyrosine Phosphorylation of Focal Adhesion Kinase at Sites in the Catalytic Domain Regulates Kinase Activity: A Role for Src Family Kinases." In: *Molecular and Cellular Biology* 15.2 (Feb. 1995), pp. 954–963. ISSN: 0270-7306.

[18] Laura Currey, Stefan Thor, and Michael Piper. "TEAD Family Transcription Factors in Development and Disease". In: *Development* 148.12 (June 2021), dev196675. ISSN: 0950-1991.

[19] Meng Sun, Fabian Spill, and Muhammad H. Zaman. "A Computational Model of YAP/TAZ Mechanosensing". In: *Biophysical Journal* 110.11 (June 2016), pp. 2540–2550. ISSN: 00063495.

[20] Kiersten Elizabeth Scott, Stephanie I. Fraley, and Padmini Rangamani. "A Spatial Model of YAP/TAZ Signaling Reveals How Stiffness, Dimensionality, and Shape Contribute to Emergent Outcomes". In: *Proceedings of the National Academy of Sciences* 118.20 (May 2021), e2021571118. ISSN: 0027-8424, 1091-6490.

[21] Emmet A. Francis and Padmini Rangamani. "Computational Modeling Establishes Mechanotransduction as a Potent Modulator of the Mammalian Circadian Clock". In: *Journal of Cell Science* 137.17 (Sept. 2024), jcs261782. ISSN: 0021-9533.

[22] Hamidreza Jafarinia et al. "Insights Gained from Computational Modeling of YAP/TAZ Signaling for Cellular Mechanotransduction". In: *npj Systems Biology and Applications* 10.1 (Aug. 2024), pp. 1–14. ISSN: 2056-7189.

[23] Emmet A. Francis et al. *Spatial Modeling Algorithms for Reactions and Transport (SMART) in Biological Cells*. May 2024.

[24] Justin G. Laughlin et al. "SMART: Spatial Modeling Algorithms for Reactions and Transport". In: *Journal of Open Source Software* 8.90 (Oct. 2023), p. 5580. ISSN: 2475-9066.

[25] Alberto Elosegui-Artola et al. "Force Triggers YAP Nuclear Entry by Regulating Transport across Nuclear Pores". In: *Cell* 171.6 (Nov. 2017), 1397–1410.e14. ISSN: 0092-8674, 1097-4172.

[26] Joe Swift et al. "Nuclear Lamin-A Scales with Tissue Stiffness and Enhances Matrix-Directed Differentiation". In: *Science* 341.6149 (Aug. 2013), p. 1240104.

[27] Newsha Koushki, Ajinkya Ghagre, Luv Kishore Srivastava, Clayton Molter, and Allen J. Ehrlicher. "Nuclear Compression Regulates YAP Spatiotemporal Fluctuations in Living Cells". In: *Proceedings of the National Academy of Sciences* 120.28 (July 2023), e2301285120.

[28] Christophe Geuzaine and Jean-François Remacle. "Gmsh: A 3-D Finite Element Mesh Generator with Built-in Pre- and Post-Processing Facilities: THE GMSH PAPER". In: *International Journal for Numerical Methods in Engineering* 79.11 (Sept. 2009), pp. 1309–1331. ISSN: 00295981.

[29] Jian Liu, Yidi Sun, David G. Drubin, and George F. Oster. "The Mechanochemistry of Endocytosis". In: *PLOS Biology* 7.9 (Sept. 2009), e1000204. ISSN: 1545-7885.

[30] Lindsey Hanson et al. "Vertical Nanopillars for in Situ Probing of Nuclear Mechanics in Adherent Cells". In: *Nature nanotechnology* 10.6 (June 2015), pp. 554–562. ISSN: 1748-3387.

[31] Kris Noel Dahl, Samuel M. Kahn, Katherine L. Wilson, and Dennis E. Discher. "The Nuclear Envelope Lamina Network Has Elasticity and a Compressibility Limit Suggestive of a Molecular Shock Absorber". In: *Journal of Cell Science* 117.20 (Sept. 2004), pp. 4779–4786. ISSN: 0021-9533.

[32] Catherine S. Hansel et al. "Nanoneedle-Mediated Stimulation of Cell Mechanotransduction Machinery". In: *ACS Nano* 13.3 (Mar. 2019), pp. 2913–2926. ISSN: 1936-0851, 1936-086X.

[33] Ana Joaquina Jimenez et al. "ESCRT Machinery Is Required for Plasma Membrane Repair". In: *Science* 343.6174 (Feb. 2014), p. 1247136.

[34] Hyejeong Seong et al. "Size-Tunable Nanoneedle Arrays for Influencing Stem Cell Morphology, Gene Expression, and Nuclear Membrane Curvature". In: *ACS Nano* 14.5 (May 2020), pp. 5371–5381. ISSN: 1936-0851.

[35] Xingpeng Di et al. "Cellular Mechanotransduction in Health and Diseases: From Molecular Mechanism to Therapeutic Targets". In: *Signal Transduction and Targeted Therapy* 8.1 (July 2023), pp. 1–32. ISSN: 2059-3635.

[36] A. Khalilimeybodi, S.i. Fraley, and P. Rangamani. "Mechanisms Underlying Divergent Relationships between Ca2+ and YAP/TAZ Signalling". In: *The Journal of Physiology* 601.3 (2023), pp. 483–515. ISSN: 1469-7793.

[37] Kerbaï Saïd Eroumé, Rachel Cavill, Katerina Staňková, Jan De Boer, and Aurélie Carlier. "Exploring the Influence of Cytosolic and Membrane FAK Activation on YAP/TAZ Nuclear Translocation". In: *Biophysical Journal* 120.20 (Oct. 2021), pp. 4360–4377. ISSN: 00063495.

[38] Hamidreza Jafarinia, Lidan Shi, Haguy Wolfenson, and Aurélie Carlier. "YAP Phosphorylation within Integrin Adhesions: Insights from a Computational Model". In: *Biophysical Journal* 0.0 (Sept. 2024). ISSN: 0006-3495.

[39] Jane H. Maduram, Edgar Goluch, Huang Hu, Chang Liu, and Milan Mrksich. "Subcellular Curvature at the Perimeter of Micropatterned Cells Influences Lamellipodial Distribution and Cell Polarity". In: *Cell motility and the cytoskeleton* 65.11 (Nov. 2008), pp. 841–852. ISSN: 0886-1544.

[40] Yuan Xiong, Chuan-Hsiang Huang, Pablo A. Iglesias, and Peter N. Devreotes. "Cells Navigate with a Local-Excitation, Global-Inhibition-Biased Excitable Network". In: *Proceedings of the National Academy of Sciences* 107.40 (Oct. 2010), pp. 17079–17086.

[41] Amalia Hadjitheodorou et al. "Directional Reorientation of Migrating Neutrophils Is Limited by Suppression of Receptor Input Signaling at the Cell Rear through Myosin II Activity". In: *Nature Communications* 12.1 (Nov. 2021), p. 6619. ISSN: 2041-1723.

[42] Fani Panagaki et al. "Structural Anisotropy Results in Mechano-Directional Transport of Proteins across Nuclear Pores". In: *Nature Physics* (May 2024), pp. 1–14. ISSN: 1745-2481.

[43] Celine M. Denais et al. "Nuclear Envelope Rupture and Repair during Cancer Cell Migration". In: *Science (New York, N.Y.)* 352.6283 (Mar. 2016), p. 353.

[44] Matthew Raab et al. "ESCRT III Repairs Nuclear Envelope Ruptures during Cell Migration to Limit DNA Damage and Cell Death". In: *Science* 352.6283 (Apr. 2016), pp. 359–362.

[45] Benoit R. Gauthier and Valentine Comaills. "Nuclear Envelope Integrity in Health and Disease: Consequences on Genome Instability and Inflammation". In: *International Journal of Molecular Sciences* 22.14 (July 2021), p. 7281. ISSN: 1422-0067.

[46] Atsuki En et al. "Pervasive Nuclear Envelope Ruptures Precede ECM Signaling and Disease Onset without Activating cGAS-STING in Lamin-cardiomyopathy Mice". In: *Cell Reports* 43.6 (June 2024). ISSN: 2211-1247.

[47] Nanxin Li, Kun Jin, Tongsheng Chen, and Xinlei Li. "A Static Force Model to Analyze the Nuclear Deformation on Cell Adhesion to Vertical Nanostructures". In: *Soft Matter* 18.35 (Sept. 2022), pp. 6638–6644. ISSN: 1744-6848.

[48] Heinrich Kovar, Lisa Bierbaumer, and Branka Radic-Sarikas. "The YAP/TAZ Pathway in Osteogenesis and Bone Sarcoma Pathogenesis". In: *Cells* 9.4 (Apr. 2020), p. 972. ISSN: 2073-4409.

[49] Christos Adamopoulos, Antonios N. Gargalionis, Christina Piperi, and Athanasios G. Papavassiliou. "Recent Advances in Mechanobiology of Osteosarcoma". In: *Journal of Cellular Biochemistry* 118.2 (2017), pp. 232–236. ISSN: 1097-4644.

[50] Stefano Piccolo, Tito Panciera, Paolo Contessotto, and Michelangelo Cordenonsi. "YAP/TAZ as Master Regulators in Cancer: Modulation, Function and Therapeutic Approaches". In: *Nature Cancer* 4.1 (Jan. 2023), pp. 9–26. ISSN: 2662-1347.

[51] Jiranuwat Sapudom et al. "Collagen Fibril Orientation Instructs Fibroblast Differentiation Via Cell Contractility". In: *Advanced Science* 10.22 (2023), p. 2301353. ISSN: 2198-3844.

[52] Britta Koch et al. "Confinement and Deformation of Single Cells and Their Nuclei Inside Size-Adapted Microtubes". In: *Advanced healthcare materials* 3.11 (Nov. 2014), pp. 1753–1758. ISSN: 2192-2640.

[53] Emmet A Francis. *SMART Nanopillars Simulation Data*. Oct. 2024.

[54] Satish Balay, William Gropp, Lois Curfman McInnes, and Barry F Smith. *PETSc, the Portable, Extensible Toolkit for Scientific Computation*. 1998.

[55] Emmet Francis, Henrik Finsberg, and Jørgen Dokken. *RangamaniLabUCSD/Smart-Nanopillars: V1.0.0*. Zenodo. Oct. 2024.

[56] Einollah Sarikhani et al. "Engineering the Cellular Microenvironment: Integrating Three-Dimensional Nontopographical and Two-Dimensional Biochemical Cues for Precise Control of Cellular Behavior". In: *ACS Nano* 18.29 (July 2024), pp. 19064–19076. ISSN: 1936-0851.

[57] San Diego Supercomputer Center. *Triton Shared Computing Cluster*. 2022. URL: https://tritoncluster.sdsc.edu (visited on 10/17/2024).